Astron. Astrophys. 364, 613–624 (2000)

ASTRONOMY AND ASTROPHYSICS

# IRAS 12326-6245: Luminous very young stellar objects with a massive molecular outflow⋆

**Th. Henning**[1], **A. Lapinov**[2], **K. Schreyer**[1], **B. Stecklum**[4], **and I. Zinchenko**[2,3]

[1] Friedrich Schiller University Jena, Astrophysical Institute and University Observatory (AIU), Schillergässchen 2-3, 07745 Jena, Germany
[2] Institute of Applied Physics of the Russian Academy of Sciences, 46 Uljanov str., 603600 Nizhny Novgorod, Russia
[3] Helsinki University Observatory, Tähtitorninmäki, P.O. Box 14, 00014 University of Helsinki, Finland
[4] Thuringian State Observatory, Sternwarte 5, 07778 Tautenburg, Germany

Received 20 March 2000 / Accepted 19 October 2000

**Abstract.** We present a comprehensive study of the luminous young stellar object IRAS 12326-6245 at near- and mid-infrared wavelengths as well as in the millimetre wavelength range.

IRAS 12326-6245 is associated with two ultracompact H II regions. These massive young stellar objects are surrounded by a cluster of stars revealed by the near-infrared images. With $N$- and $Q$-band imaging, we find four very deeply embedded mid-infrared sources which form a remarkable proto-Trapezium system. Both ultracompact H II regions are associated with mid-infrared sources. In addition, a $K'$-band nebulosity is present which outlines the rim of the molecular outflow.

The mapping in different molecular lines as well as in the $\lambda$ 1.3 mm continuum shows that IRAS 12326-6245 is deeply embedded in a dense molecular cloud core in agreement with the steeply rising infrared spectral energy distributions of the ultracompact H II regions. In the region one of the most energetic and massive bipolar molecular outflows was detected in CO(2–1), $C^{18}O$(2–1), and SO with its origin close to IRAS 12326-6245.

**Key words:** stars: formation – ISM: clouds – ISM: individual objects: IRAS 12326-6245 – ISM: molecules – radio lines: ISM

## 1. Introduction

Massive stars strongly influence the dynamical and chemical evolution of the interstellar medium. The formation of massive stars may lead both to a destruction of molecular cloud cores and disks around young stars by their intense UV radiation and strong outflows and to shock waves which may trigger the formation of a new generation of stars.

Despite the importance of massive stars, we do not know if they form by accretion (see, e.g., Jijina & Adams 1996) or/and the coalescence of intermediate-mass stars (Bonnell et al. 1998). The detection of disks around and outflows from massive young stellar objects (YSOs) would favour the accretion scenario. This is a strong motivation for our search of energetic outflows associated with such objects. In a recent very comprehensive review, Garay & Lizano (1999) summarized evidence for the presence of disk-like structures and outflows associated with massive YSOs.

The few outflows from massive star-forming regions detected so far are much more energetic and carry more mass and momentum than outflows from low-mass stars (Shepherd & Churchwell 1996a,b; Shepherd et al. 1998; Henning et al. 2000b). In this paper, we report the detection of a very massive molecular outflow and discuss the properties of the driving source.

IRAS 12326-6245 is known as a luminous far-infrared source with a bolometric luminosity of $L_{\rm bol}$ = 3.8 $10^5$ $L_\odot$ at a kinematically estimated distance of $d = 4.4$ kpc (Zinchenko et al. 1995; Osterloh et al. 1997). This distance is adopted throughout the paper.

This remarkable object is associated with several molecular masers including $H_2O$, OH and methanol masers (e.g. Braz & Epchtein 1983, 1987; Caswell & Haynes 1987; Cohen et al. 1988; Caswell et al. 1995; MacLeod et al. 1998) which were found at the position of IRAS 12326-6245. However, most of these measurements were performed with beam sizes larger than 2 arcmin. Recent interferometer observations by Caswell (1998) show an OH maser very close to the IRAS position. Although Walsh et al. (1998) reported the presence of two UC H II regions close to the IRAS position, they detected no 6.7 GHz methanol maser emission (resolution 1.8″) in the region of IRAS 12326-6245.

Strong thermal molecular emission towards IRAS 12326–6245 was mapped in CS(2–1) and CO(2–1) by Zinchenko et al. (1995) and Osterloh et al. (1997) as well as in CS(3–2), $C^{34}S$(2–1) and $C^{18}O$(1–0) by Lapinov et al. (1998). These maps show that the dense molecular core is compact ($\sim 1'$) and elongated approximately in the E–W direction. The CO spectra exhibit extended wings suggesting the presence of a massive molecular outflow. In a beam of 23″, a cloud mass of 320 $M_\odot$ was derived by Osterloh et al. (1997).

*Send offprint requests to*: Th. Henning

⋆ Based on observations collected at the European Southern Observatory, La Silla, Chile

*Correspondence to*: henning@astro.uni-jena.de

Wood & Churchwell (1989) defined a "very red" region in the IRAS $\log[S_\nu(60\mu m)/S_\nu(12\mu m)]$ versus $\log[S_\nu(25\mu m)/S_\nu(12\mu m)]$ colour diagram, where UC H II regions are located. The comparison of the colours of IRAS 12326–6245, having $\log[S_\nu(60\mu m)/S_\nu(12\mu m)]$ = 2.99 and $\log[S_\nu(25\mu m)/S_\nu(12\mu m)]$ = 1.60, with this region demonstrates that IRAS 12326–6245 is an extremely red and cold object (see also Osterloh et al. 1997).

In general, the available data imply a rather isolated region of high-mass star formation at an early stage. According to available distance estimates it is located almost 10 times farther away than the Orion Molecular Cloud, but the intensities of the line emission are comparable. The goal of the present study is to investigate in more detail this remarkable object. Here, we report the results of additional observations of IRAS 12326–6245 in the near- and mid-infrared, in several molecular lines as well as in the 1.3 mm continuum emission, and we discuss the whole available data set.

## 2. Observations

### 2.1. Molecular observations

The observations were performed in 1996–1997 with the 15-m SEST telescope on La Silla, Chile. The telescope and its instrumentation are described by Booth et al. (1989). The most important parameters of our measurements are summarized in Table 1. Further details are given below.

The observations were performed with SIS receivers in a single-sideband mode. At 220 GHz, we used dual beam switching with a beam throw of $\sim 12'$ and 2 acousto-optical spectrometers in parallel: (1) a 2000 channel high-resolution spectrometer with a 86 MHz bandwidth, 43 kHz channel separation and 80 kHz resolution and (2) a 1440 channel low-resolution spectrometer (LR1) with a 1000 MHz total bandwidth, 0.7 MHz channel separation, and 1.4 MHz spectral resolution. The LR1 band was centered on the HNCO($10_{0,10}$–$9_{0,9}$) transition. However, it also covered $C^{18}O$(2–1), SO($6_5$–$5_4$) and other lines (see Table 1). The $C^{34}S$(3–2) measurements at 145 GHz were made in a dual beam switching mode, too, using a high-resolution spectrometer as backend. The beam size is 23″ (HPBW) at 230 GHz and 35″ at 145 GHz.

Throughout the paper, we adopt the IRAS co-ordinates as the central source position ($\alpha(1950) = 12^{\rm h}32^{\rm m}41\overset{\rm s}{.}0$, $\delta(1950) = -62°45'57''$). The area of 40″×40″ around this position was mapped with 10″ spacing in SO($6_5$–$5_4$), $C^{18}O$(2–1), and HNCO($10_{0,10}$–$9_{0,9}$) and with 15″ spacing in $C^{34}S$(3–2). The peak position was also observed in $^{34}$SO($6_5$–$5_4$).

The CO(2–1) map for IRAS 12326–6245 was sampled with 2/3 beamwidth intervals of 15″. The observations were made in the position-switch mode with an OFF position of 30′ to the east and an integration time of 30 seconds per ON and per OFF position. Based on the repeated measurements of smaller parts of the map, the total integration time per ON position ranged between 1 minute and 3.5 minutes, resulting in a $T_{\rm mb}$(rms) between 0.18 and 0.46 K. The pointing was checked every two to three hours with the source W Hya and was found to be accurate to better than 6″.

**Table 1.** Parameters of molecular line observations

| Molecule | Transition | Frequency (MHz) | $T_{\rm sys}^{*1}$ (K) | $\Delta\nu$ (kHz) |
|---|---|---|---|---|
| CO | $2-1$ | 230537.990 | 300–350 | 86 |
| HNCO | $10_{0,10}-9_{0,9}$ | 219798.320 | 190–240 | 86 |
| $C^{18}O$ | $2-1$ | 219560.319 | 190–240 | 1400 |
| SO | $6_5-5_4$ | 219949.442 | 190–240 | 1400 |
| $^{34}$SO | $6_5-5_4$ | 215839.436 | 270 | 86 |
| $C^{34}S$ | $3-2$ | 144617.147 | 170 | 86 |

$^{*1}$ The system temperatures are given in the $T_{\rm A}^*$ scale.

We express the results in units of the main beam brightness temperature ($T_{\rm mb}$) assuming the main beam efficiencies $\eta_{\rm mb} = 0.50$ at 230 GHz and 0.52 at 220 GHz. The temperature scale was checked by observations of Orion A.

### 2.2. Bolometer observations

The continuum observations were performed in March 1996 with the one-channel $He^3$-cooled SEST facility bolometer (Kreysa 1990). The bolometer has an equivalent bandwidth of ≈ 50 GHz and a central frequency of $\nu_0$ = 236 GHz ($\lambda_0$ = 1.27 mm). The beam size at this wavelength is 23″ (HPBW).

The maps were obtained with the standard "double beam" technique (Emerson et al. 1979), i.e. by scanning the telescope continuously in azimuth over the source position while chopping with a frequency of 6 Hz and a beam throw of 67″ in scan direction. The beam switching was performed with a focal plane chopper. A scanning velocity of 8″/second was used and the elevation spacing between adjacent scans was 8″.

Three individual maps with a size of $5'\times 4'$ were combined to produce the final map of the source. The atmospheric transmission was measured by sky dips and amounted to $\tau_{1.3\rm mm} = 0.15\ldots0.25$ during the whole observing run. Telescope pointing and focus were checked frequently towards nearby quasars. The pointing was repeatable within 5″. Uranus served as calibration standard, adopting a brightness temperature of 96 K (Griffin & Orton 1993). The average 1 $\sigma$ rms noise in the final map (outside the source) is 48 mJy/beam. Data reduction was performed with the MOPSI software package (R. Zylka).

### 2.3. Imaging in $H$, $J$, $K'$, and $H_2$

The near-infrared (NIR) broad- and narrow-band imaging was performed using IRAC2b (Moorwood et al. 1992) at the ESO 2.2-m telescope in June, 1998, during the time slot alloted to the Max-Planck-Institut (MPI), Heidelberg. Dithered images were taken at five positions yielding an overall field-of-view of about 160″×160″. The resulting total integration times for the central region are as follows: 800 s ($J$), 400 s ($H$), 200 s ($K'$), and 20 minutes for the narrow-band filters BP4 (continuum, 2.105 $\mu$m) and $H_2$ (2.122 $\mu$m). The limiting magnitudes (3 $\sigma$ point source

detection) of the J, H, and $K'$ images are 17, 18, and 18.5 mag, respectively. In order to obtain a continuum-subtracted $H_2$ image, the BP4 image was convolved to match the point spread function (PSF) of the $H_2$ image. After this step, the continuum emission was subtracted from the $H_2$ image. Nevertheless, residuals of bright stars are still present in the subtracted image (Fig. 2b).

The intrinsic image scale of lens C ($0\farcs5$) was resampled to $0\farcs25$ during the mosaicking of the final image. The angular resolution as derived from stellar profiles is $1''$. The astrometry is based on stellar positions extracted from the DSS2 image of the region and is accurate to $\sim 1''$.

### *2.4. $N$- and $Q$-band imaging*

Diffraction limited thermal-infrared images were obtained in March, 1998 during Max Planck time using MANIAC (Böker et al. 1997) at the ESO 2.2-m telescope. The observations were performed with the common chopping/nodding technique at a pixel scale of $0\farcs345$ and a total on-source integration time of 3.5 min. A chopper throw of $30''$ was applied. The individual images were subject to a wavelet-filtering algorithm (Pantin & Starck 1996) which preserves both flux and spatial resolution while suppressing the noise considerably. These images were then resampled to half the original pixel size and combined using a shift-and-add algorithm to compensate for image motion. The coarse astrometry derived using the telescope offsets from the reference star indicated that two infrared sources are close to the unresolved ultracompact H II regions found by Walsh et al. (1998). Thus, the final astrometry was tied to the radio positions. The $N$ and $Q$ band photometry of the detected sources (above 3 $\sigma$ noise level) is based on the 12.13 $\mu$m and 21.34 $\mu$m MSX flux densities. The 3 $\sigma$ detections limits are 0.16 Jy in $N$ and 11 Jy in $Q$, respectively. The individual flux contributions were derived using a multi-component PSF fitting algorithm. The MIR source 4 is either a binary or is associated with extended emission. For the derivation of the flux, it was treated as a binary source. We should stress that MIR3 is present in the $Q$ band image at a 2 $\sigma$ level.

We also added mid-infrared data from the MSX-SPIRIT III point source catalog (Egan et al. 1999). The 1 $\sigma$ error ellipse of the point sources detected by MSX in the field is $1\farcs1 \times 1\farcs4$.

## 3. Results

### *3.1. Infrared data*

The Figs. 1 and 2 show the region of IRAS 12326–6245 in the optical, the near-, and the mid-infrared wavelength range. The R-band image indicates the external illumination of the northern rim of the molecular cloud.

The near-infrared images clearly reveal the presence of a stellar cluster around the UC H II regions. The radial stellar surface density was derived from the $K'$ image (Fig. 1) which has the best spatial resolution by applying annuli centered on the southern UC H II region. The resulting distribution (Fig. 3) shows four distinct regions. Beyond the central density enhancement due to the embedded cluster, a region of reduced surface density is obvious, which corresponds to the area of the molecular cloud core. In this region, background stars are diminished because of the extinction by the molecular cloud. The boundary of the cloud is obvious from the increase of the stellar surface density which finally drops because of the finite size of the field. From the stellar surface density, we derive a lower limit for the volume density of 123 stars per pc$^3$ within a sphere of radius 0.43 pc. We should note that most of the cluster members seen at near-infrared wavelengths are located in front of the molecular cloud core or at its surface because the total extinction derived from the millimeter data amounts to 200–600 mag. The extinction over the cluster varies, which implies that multi-object spectroscopy is needed for the derivation of a reliable colour-magnitude diagram.

In the 2.2 $\mu$m broad- and narrow-band images (see Figs. 1d, 2a,b), an infrared nebula is present with the apex near the northern UC H II region. Most of the emission is scattered light. The nebula is located at the border of the molecular outflow discussed in Sect. 3.3. It may be the illuminated rim of this flow.

The $H_2$ image (Fig. 2b) shows three knots north of the brightest star (located in the centre of the image) as well as a bow-shaped feature. The comparison of Fig. 2a with Fig. 2b demonstrates that these structures are not produced by light scattering. They are located in a region which may be related to the northwestern part of the molecular outflow. However without further spectroscopic information, we cannot distinguish between shock excitation or fluorescence producing this emission.

In the $N$-band image (Fig. 2c) four objects have been detected which are not present in the $K'$ image. Therefore, these sources must be much more deeply embedded and presumably resemble a proto-Trapezium system. With a lower limit for the assumed $Q$- to $N$-band flux ratio of 10 (see, e.g., Henning et al. 2000b) for deeply embedded sources, we would expect $Q$ flux values for MIR 3 of 8 Jy and for MIR 4 of 5 Jy, respectively. The flux for MIR 3 is about the 2 $\sigma$ detection limit which well fits the fact that this source is just seen at this level in the $Q$ band. MIR 4 could not be detected with the sensitivity of our observations.

The positions of the northern and the strongest southern peak in the $N$- and $Q$-band images agree well with those of the unresolved ultracompact H II regions found by Walsh et al. (1998) at 6.67 and 8.64 GHz. The projected distance of these two objects is about 25000 AU which is well within the maximal extent of Trapezium systems with OB primary stars given by Abt (1986). We should note that this is one of the first detections of such a deeply embedded Trapezium system.

The IRAS position uncertainty is rather high and the IRAS source can probably be identified with the southern source although both infrared objects contribute to the IRAS fluxes. The intrinsic fluxes of the individual sources can be better constrained by the MSX data in combination with our MANIAC images. The northern MSX source in the field is coincident with the IRAS source and clearly located at the position of the strongest mid-infrared source MIR 1. Here, we should note that

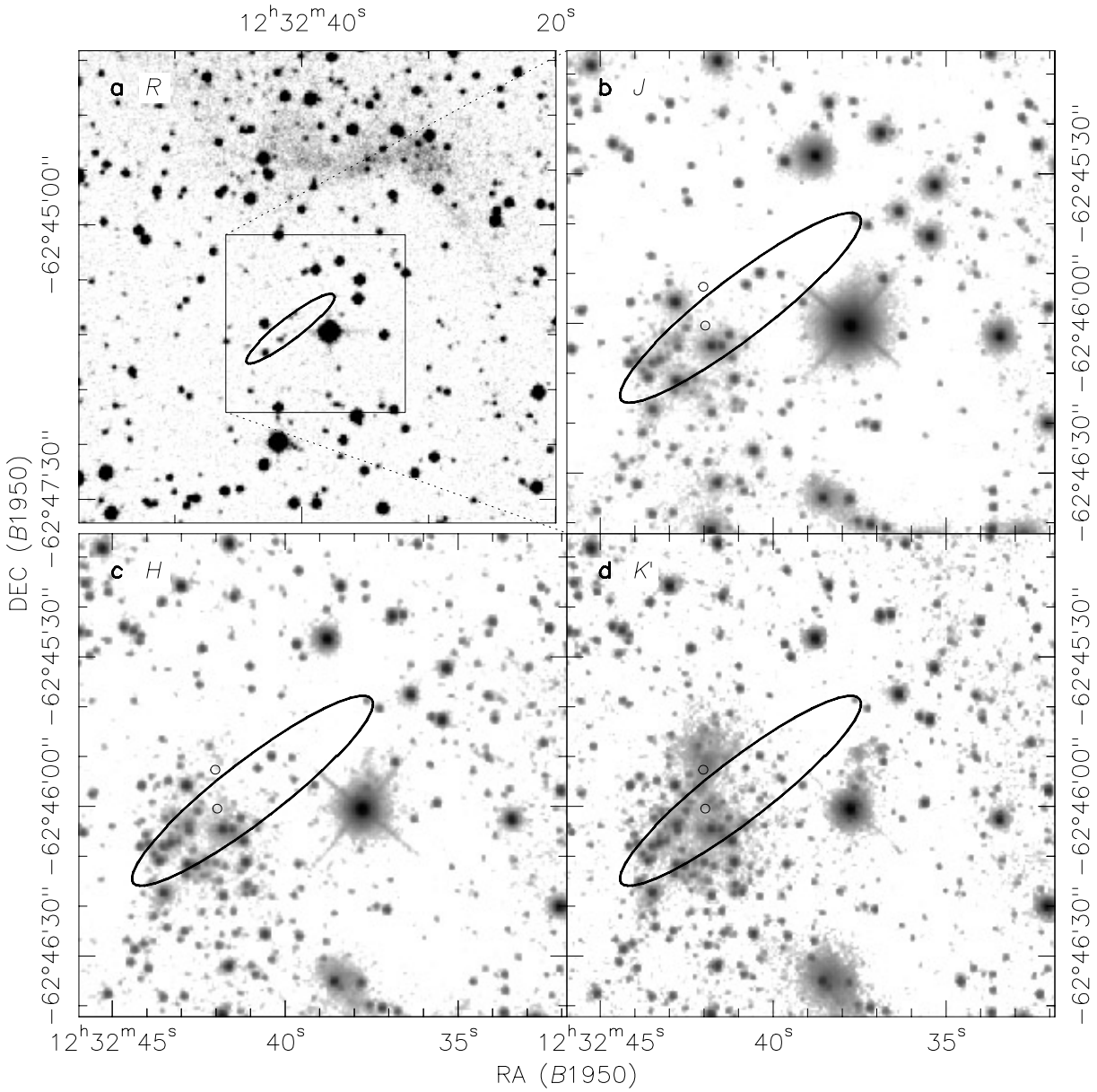


**Fig. 1a–c.** The region of IRAS 12326–6245 seen in **a** $R$-band (ESO Survey), **b** $J$-band, **c** $H$-band, and **d** $K'$-band. The open circles show the positions of the ultracompact H II regions (Walsh et al. 1998). The thick ellipses indicate the IRAS error ellipse.

MSX provided a much better positional accuracy and a smaller error ellipse (see Fig. 2). The MSX positions and fluxes are compiled in Tables 2 and 3. Table 4 summarizes the photometry of the mid-infrared sources. The comparison of the $N$- and $Q$-band fluxes of the mid-infrared sources MIR 1 and 2 shows a steep increase of the spectral energy distribution towards longer wavelengths with a similar flux ratio.

### *3.2. Structure of the region at millimetre wavelengths*

The Figs. 4 and 5 show the overall structure of the region around IRAS 12326–6245 as seen in the molecular lines as well as in the 1.3 mm continuum. In Fig. 4, the $^{12}$CO(2–1) and the 1.3 mm continuum measurements are superimposed on the $R$-band image and the $K$-band image, respectively. Both maps indicate the presence of a dense cloud core surrounded by a more extended envelope with lower emission. In both cases, we studied a region of roughly $60'' \times 60''$ which covers the cloud center only. A large-scale overview can be obtained by IRAS maps which show a spherical cloud structure with an extension of roughly $5' \times 4.3'$. These maps are not shown in the paper because they only show the rather symmetric infrared emission.

IRAS 12326–6245 is characterized by very strong 1.3 mm continuum emission comparable in strength with the sources discussed by Henning et al. (2000a). The emission peaks at the IRAS position. The Gaussian core profile is barely resolved in the NE–SW direction and remains unresolved in the NW–SE direction. The 1.3 mm peak flux density and the 1 $\sigma_{\rm rms}$ noise value

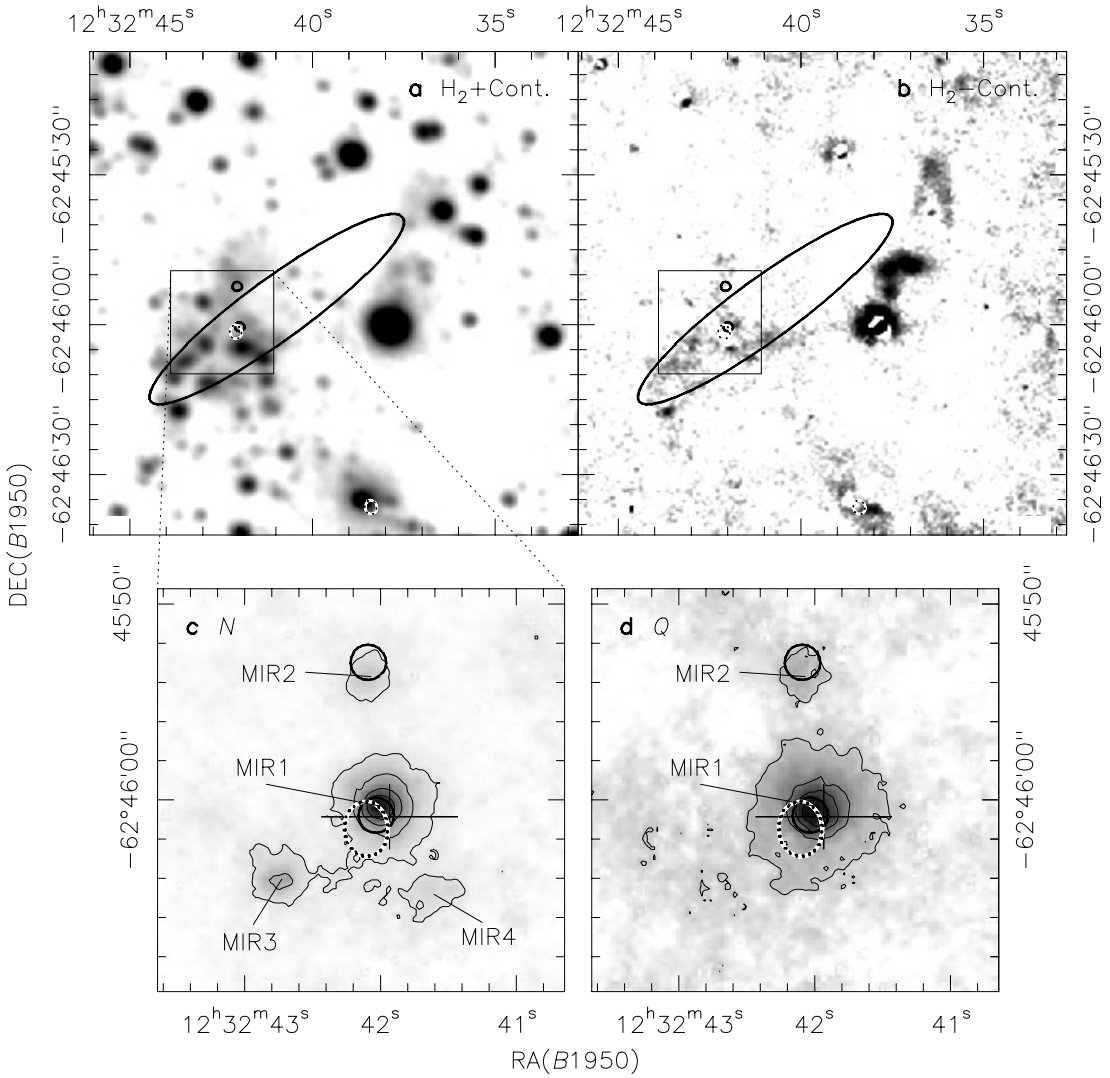


**Fig. 2a–d.** The region of IRAS 12326–6245 shown in the **a** $H_2$ (2.12$\mu$m) emission, **b** $H_2$ (2.12$\mu$m) emission (continuum subtracted), **c** $N$-band (10$\mu$m), and **d** $Q$–band (20$\mu$m) emission. The open circles label the positions of the ultracompact H II (UC H II) regions (Walsh et al. 1998) and the crosses give the 1.67 GHz OH maser position by Caswell (1998), whereby the lengths of the cross axes indicate their synthesized beam size. The thick ellipses show the IRAS error ellipse. The dotted ellipses mark the positions of the two MSX sources (see Table 2). The contour levels in the $N$-band image are 15%(=2$\sigma$), 25%, 40%, and 60% of the peak emission. In the $Q$-band, the levels indicate 20%(=4$\sigma$), 40%, 60% and 80% of the peak emission.

amount to 9.3 Jy/beam and 15 mJy/beam, respectively. The peak flux density agrees well with the earlier On-Off measurement by Osterloh et al. (1997). The total 1.3 mm flux density $S_\nu^{\rm total}$ was obtained by integrating the observed millimeter flux density (surface brightness) of the map within the 3 $\sigma_{\rm rms}$ contour (2.88 □′). In order to estimate the core flux density $S_\nu^{\rm core}$, the central component was fitted by a 2-dimensional Gaussian and the integrated flux density within this Gaussian was determined separately. The results are $S_\nu^{\rm total}$ = 26.4 Jy and $S_\nu^{\rm core}$ = 12.0 Jy for the total flux and the core flux, respectively.

In Fig. 5, we present the integrated intensity maps of the $C^{18}O$(2–1), SO($6_5$–$5_4$), and $C^{34}S$(3–2) measurements as gray scale images. Whereas the emission in $C^{18}O$ is somewhat more extended as the image shown, the SO and the $C^{34}S$ measurements roughly cover the whole dense core emission. We should note that the intensity peaks of the $C^{18}O$ and SO maps are shifted to the eastern side of the southern UC H II region, whereas the peak positions in CO and the 1.3 mm continuum are shifted to the western side (peak separation $\approx 12''$). The emission of $C^{34}S$ peaks 7″ to the south of the southern UC H II region. These shifts are very probably caused by the pointing inaccuracy of the SEST telescope. Summarizing the results, we find that the molecular line emission peaks very close to the position of the southern UC H II region being the most prominent object at mid-infrared wavelengths. The HNCO emission is spatially unresolved with the SEST 23″ beam. This is in agreement with the fact that the HNCO molecule traces the densest parts of molecular clouds (see, e.g., Jackson et al. 1984).

**Table 2.** Coordinates of the sources in the region of IRAS 12326-6245

| name | coordinates ($B$1950) | |
|---|---|---|
| | RA (h : m : s) | DEC ($^\circ$ : $'$ : $''$) |
| IRAS 12326−6245 | 12:32:41.0 | −62:45:57 |
| MSX5C G301.1365–00.2257 | 12:32:42.1 | −62:46:01.5 |
| MSX5C G301.1302–00.2360[*1] | 12:32:38.40 | −62:46:36.7 |
| northern UC H II[*2] | 12:32:42.09 | −62:45:53.0 |
| southern UC H II[*2] | 12:32:42.03 | −62:46:00.5 |

[*1] Object can be identified with a stellar source, probably an evolved star with a circumstellar envelope. It is contained in the U.S. Naval Observatory (USNO) catalog.
[*2] Positions after Walsh et al. (1998).

**Table 3.** Fluxes of MSX5C G301.1365–00.2257 which seems to be coincident with IRAS 12326–6245

| $\lambda$ [$\mu$m] | flux density [Jy] | $\lambda$ [$\mu$m] | flux density [Jy] |
|---|---|---|---|
| 8.28 | $< 0.093$ | IRAS 12 | 7.79: |
| 12.13 | 5.2 ($\pm$0.2) | IRAS 25 | 308.9 |
| 14.65 | 17.9 ($\pm$0.7) | IRAS 60 | 7557.0 |
| 21.34 | 147.0 ($\pm$8.8) | IRAS 100 | 9296.0 |

**Table 4.** Photometry in the $N$- and $Q$-bands

| object | coordinates ($B$1950) | | flux |
|---|---|---|---|
| | RA(h : m : s) | DEC($^\circ$ : $'$ : $''$) | [Jy] |
| | $N$-band | | |
| MIR 1 (south. UC H II) | 12:32:42.10 | −62:46:00.4 | 3.46±0.09 |
| MIR 2 (north. UC H II) | 12:32:42.02 | −62:45:53.7 | 0.48±0.06 |
| MIR 3 (east) | 12:32:42.74 | −62:46:03.9 | 0.76±0.09 |
| MIR 4 (west) | 12:32:41.62 | −62:46:04.7 | 0.49±0.14 |
| | $Q$-band | | |
| MIR 1 | 12:32:42.00 | −62:46:00.4 | 123±5 |
| MIR 2 | 12:32:42.11 | −62:45:53.6 | 24±5 |

In addition, we fitted the line profiles with single Gaussian profiles at the peak positions of each molecular line species. The fits results of the values $V_{LSR}$, $T_{mb}$, $\Delta V$, and $\int T_{mb} dv$ are compiled in Table 6.

### *3.3. Outflow*

The spectra in CO(2–1), $C^{18}O$(2–1), SO($6_5$–$5_4$), $^{34}$SO($6_5$–$5_4$), and $C^{34}S$(3–2) at the peak position are presented in Fig. 6. The CO and SO spectra are obviously characterized by extended wings. The wing component is also present in the $C^{18}O$(2–1) line. However, no non-Gaussian wings are seen in the $C^{34}S$(3–2) spectrum.

In the Figs. 4a and 5, we overlaid the integrated intensities of the corresponding red- and blue-shifted line emissions in CO, $C^{18}O$, and SO. A more detailed discussion of the properties as well as the estimate of physical parameters of the outflow are given in Sect. 4.3.

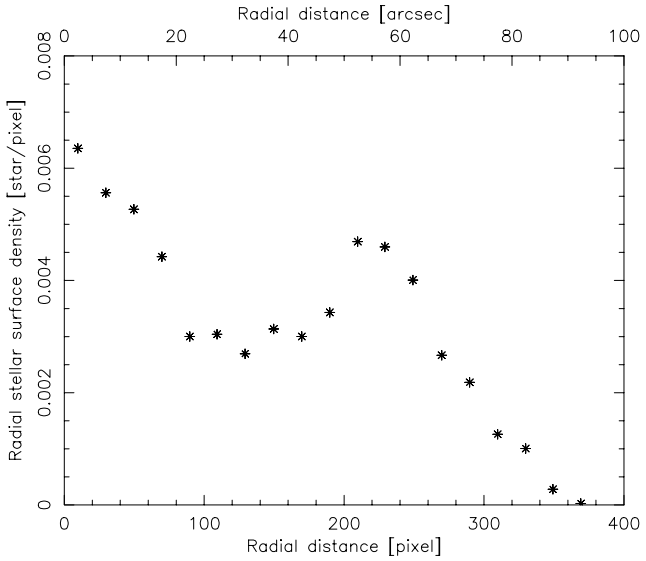


**Fig. 3.** Radial surface density of the stars in the $K'$ image. The annuli were centered on the position of the southern UC H II region. The distribution can be subdivided into four regions: $r < 80$ pixel: radial density profile of the embedded stellar cluster, 80 pixel $< r <$ 200 pixel: reduced background density due to the extinction of the molecular cloud core, 200 pixel $< r <$ 230 pixel: "normal" background density, $r > 230$ pixel: decreasing density due to finite field size.

## 4. Discussion

### *4.1. General properties*

IRAS 12326–6245 is associated with maser emission and with at least one of the two UC H II regions indicated in the Figs. 2–5.

Both phenomena are usually associated with the presence of very young massive stars. However, the UC H II regions remained unresolved with arcsec resolution (Walsh et al. 1998). This indicates that either the regions have a large distance or that they are very young. The UC H II regions have sizes smaller than $6\,10^3$ AU which is rather small compared with other well-known UC H II regions, like G5.89-0.39.

Based on the free-free continuum emission measured by Walsh et al. (1998), we derived the brightness temperature $T_b$, the optical depth $\tau$, the emission measure EM, the electron density $n_e$, the excitation parameter $U$, and the Lyman continuum photon flux $L_c$ (see Wood & Churchwell 1989). Using the calibration by Vacca et al. (1996) and assuming a *single* star as the excitation source for each of the UC H II regions, we obtain a spectral type B0 or earlier if dust extinction in the UC H II regions is important. This gives a luminosity of $8\,10^4$ $L_\odot$ for the individual objects. The total luminosity derived from the IRAS and MSX measurements amounts to $3\,10^5$ $L_\odot$ in good agreement with the estimates of the radio data.

Fig. 7 displays the spectral energy distribution (SED) of IRAS 12326–6245 taking into account the IRAS data, our infrared, and $\lambda$ 1.3 mm continuum data. The data can be well fitted by a modified Planck function (1–exp($-\tau(\lambda)$))$B_\lambda(\lambda, T)$ with $\tau(\lambda) \propto \lambda^{-\beta}$. The parameters of the fit are a temperature of 60±7 K and an index $\beta$ for the wavelength-dependent absorptivity of

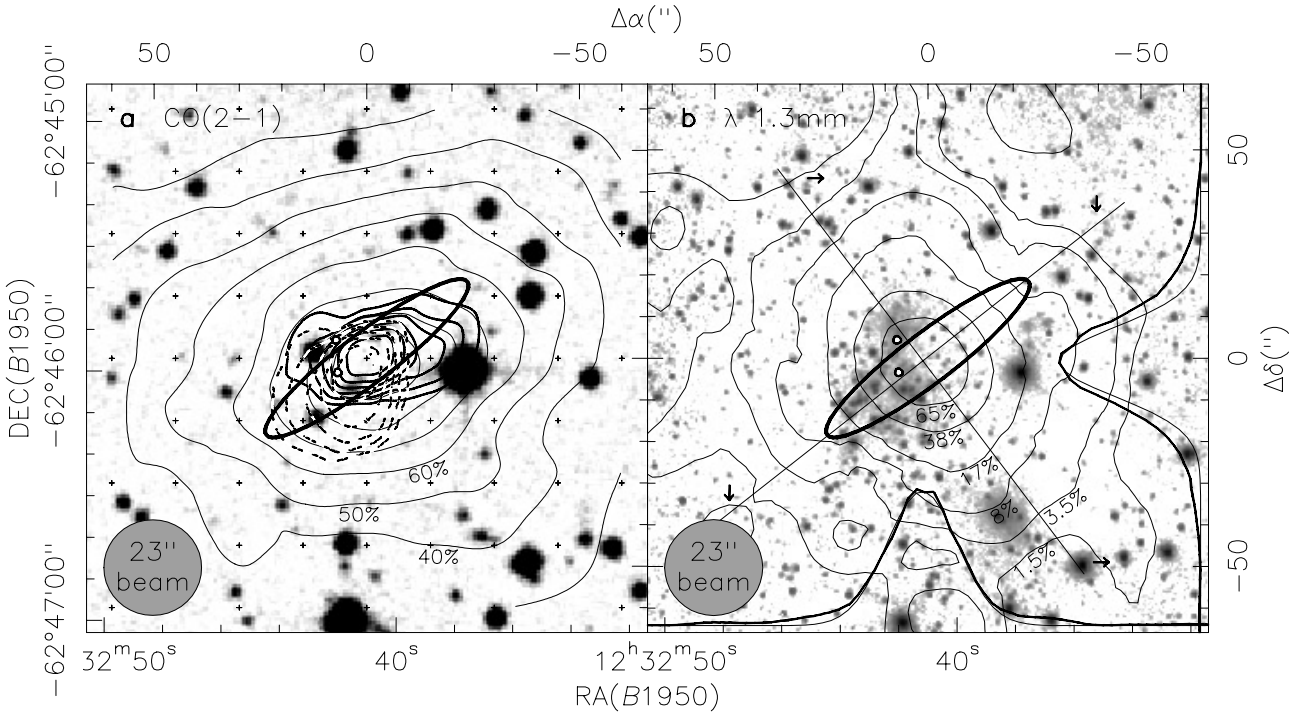


**Fig. 4.** **a** The CO (2–1) measurements of IRAS 12326–6245 are superimposed on the $R$-band image (Fig. 1a). The integrated intensity map of the CO line ($-47$ km s$^{-1}$ $\leq$ v$_{\rm LSR}$ $\leq$ $-33.5$ km s$^{-1}$) is shown with thin contour lines (peak 288 K km s$^{-1}$). The integrated intensities of the red-shifted ($-32$ km s$^{-1}$ $\leq$ v$_{\rm LSR}$ $\leq$ $-11.5$ km s$^{-1}$; thick dashed contour lines) and the blue-shifted CO line wings ($-71$ km s$^{-1}$ $\leq$ v$_{\rm LSR}$ $\leq$ $-47$ km s$^{-1}$; thick solid contour lines) are overlaid. Contour levels are 40 to 90% by steps of 10% of the peak emissions (blue: 62 K km s$^{-1}$; red: 68 K km s$^{-1}$). The small crosses indicate the positions of the measurements. **b** The map of the $\lambda$ 1300 $\mu$m dust emission (contour levels with a logarithmic intensity scale, peak value = 9.4 Jy/beam) is superimposed on the $K$-band image (Fig. 1d). Cuts through the intensity distribution along the major and the minor axis are overplotted with thick lines, whereby the Gaussian beam profile is overlaid with thin lines. The open circles in both figures label the position of the ultracompact H II regions found by Walsh et al. (1998). The beam sizes are indicated by a grey circle in the lower left, and the thick ellipses are the IRAS error ellipse.

**Table 5.** Parameters of the UC H II regions determined from the free-free continuum measured by Walsh et al. (1998) using an electron temperature of $T_e$ = 1 10$^4$ K and unresolved beam sizes of 1.5″ at 8.64 GHz and 1.9″ at 6.67 GHz.

| $\nu$ [GHz] | flux density [mJy/beam] | $T_{\rm b}$ [K] | $\tau$ | EM [pc cm$^{-6}$] | $n_{\rm e}$ [cm$^{-3}$] | U [pc cm$^{-2}$] | $L_{\rm c}$ [s$^{-1}$] |
|---|---|---|---|---|---|---|---|
| southern UC H II region | | | | | | | |
| 190 | 6.67 | 1450 | 0.16 | 2.6 10$^7$ | 2.5 10$^4$ | 34.84 | 1.35 10$^{48}$ |
| 210 | 8.64 | 1533 | 0.17 | 4.7 10$^7$ | 3.8 10$^4$ | 36.39 | 1.54 10$^{48}$ |
| northern UC H II region | | | | | | | |
| 230 | 6.67 | 1755 | 0.19 | 3.2 10$^7$ | 2.8 10$^4$ | 37.34 | 1.67 10$^{48}$ |
| 170 | 8.64 | 1240 | 0.13 | 3.7 10$^7$ | 3.4 10$^4$ | 33.73 | 1.23 10$^{48}$ |

1.2±0.5. The luminosity amounts to $L_{\rm bol}$ = 3.4±1.0 10$^5$ L$_\odot$. We note that the region has a very complex structure. Therefore, the use of a single modified black-body function is certainly oversimplified. In principle, we expect a distribution of temperatures inside the considered area. However, a radiative transfer calculation would require spatially resolved data to constrain the adopted model. The SED is similar to the SEDs of other UC H II regions (e.g. W 3(OH); Chini et al. 1986), but with less flux at near-infrared wavelengths pointing again to deeply embedded sources. This is clearly different to the BN-type objects (e.g. AFGL 490) which show even more near-infrared emission (Henning et al. 1990, 2000b; Gürtler et al. 1991).

### *4.2. Physical parameters of the core and envelope*

Using the $\lambda$ 1.3mm continuum measurements as well as the molecular line maps, we can estimate physical parameters as the column densities, the volume-averaged hydrogen number densities, and the masses of central cloud core as well as the total mass of the molecular cloud associated with IRAS 12326–6245.

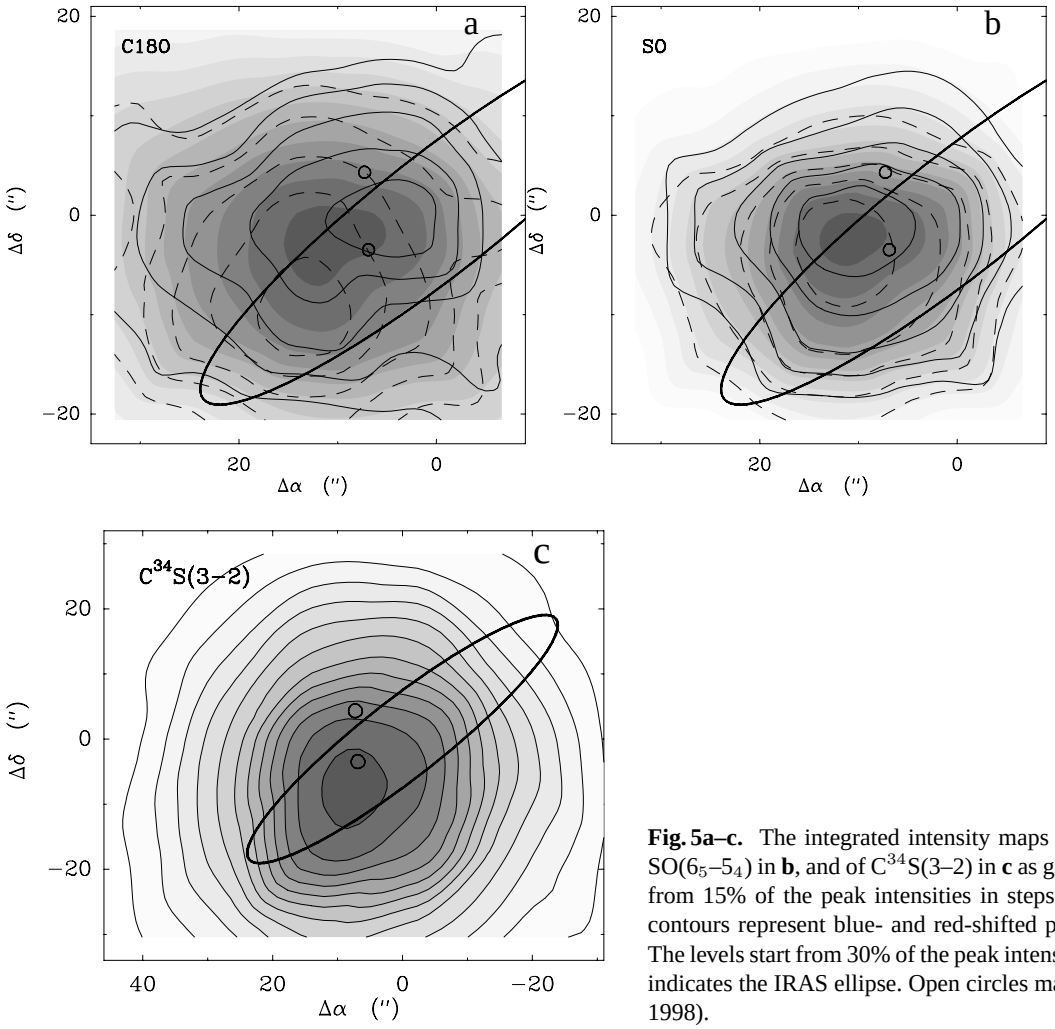


**Fig. 5a–c.** The integrated intensity maps of $C^{18}O(2–1)$ is shown in **a**, of $SO(6_5–5_4)$ in **b**, and of $C^{34}S(3–2)$ in **c** as grey scale images. The levels start from 15% of the peak intensities in steps of 7.5%. The solid and dashed contours represent blue- and red-shifted parts of the spectra, respectively. The levels start from 30% of the peak intensities in steps of 15%. The ellipse indicates the IRAS ellipse. Open circles mark UC H II regions (Walsh et al. 1998).

**Table 6.** Results of molecular line observations for the position of the intensity peaks

| Molecule | Transition | rms[*1] (K) | $V_{LSR}$ (km s$^{-1}$) | $T_{mb}$ (K) | $\Delta V$ (km s$^{-1}$) | $\int T_{mb} dv$ (K km s$^{-1}$) |
|---|---|---|---|---|---|---|
| CO | $2-1$ | 0.2 | $-39.8$ | 43.6[*2] | 8.7 | 405.0 |
| $C^{18}O$ | $2-1$ | 0.02 | $-40.0$ | 7.1 | 5.4 | 44.35 |
| SO (a) | $6_5-5_4$ | 0.02 | $-38.5$ | 4.7 | 6.0 | 30.20 |
| SO (b) | $6_5-5_4$ | 0.02 | $-38.9$ | 1.5 | 21.4 | 34.20 |
| $^{34}SO$ | $6_5-5_4$ | 0.08 | $-39.4$ | 1.2 | 6.5 | 8.11 |
| $C^{34}S$ | $3-2$ | 0.1 | $-39.3$ | 2.7 | 4.7 | 13.70 |
| HNCO | $10_{0,10}-9_{0,9}$ | 0.04 | $-39.4$ | 0.6 | 6.4 | 4.15 |

[*1]The values are given in scale of $T_{mb}$.
[*2]Fit with mask in order to cover the absorption features and the non-Gaussian line wings.

The $H_2$ column density and the mass can be derived from the 1.3 mm continuum observations under the assumptions that the emission is completely dominated by thermal dust radiation (see, e.g., Watson et al. 1997) and that it is optically thin. The first assumption is fully justified when the low free-free emission at millimetre wavelengths, extrapolated from the radio data, is considered. The total gas mass is $M_{gas}^{total} \approx 11900$ M$_\odot$ and the core has a mass of $M_{gas}^{core} \approx 2400$ M$_\odot$. Here, we used a gas-to-dust mass ratio of 150 based on solar metallicity and a correction factor of 1.36 to account for He and metals. For the mass absorption coefficient of the dust $\kappa_m^d$, we chose values of $\kappa_m$(1.3mm) = 0.9 cm$^2$ g$^{-1}$ for the dense core and $\kappa_m$(1.3mm) = 0.5 cm$^2$ g$^{-1}$ for the envelope (Ossenkopf & Henning 1994) which refer to coagulated dust particles with thin ice mantles in high and intermediate dense protostellar cores. Following Henning et al. (2000a), we applied a 'beam-averaged' dust temperature

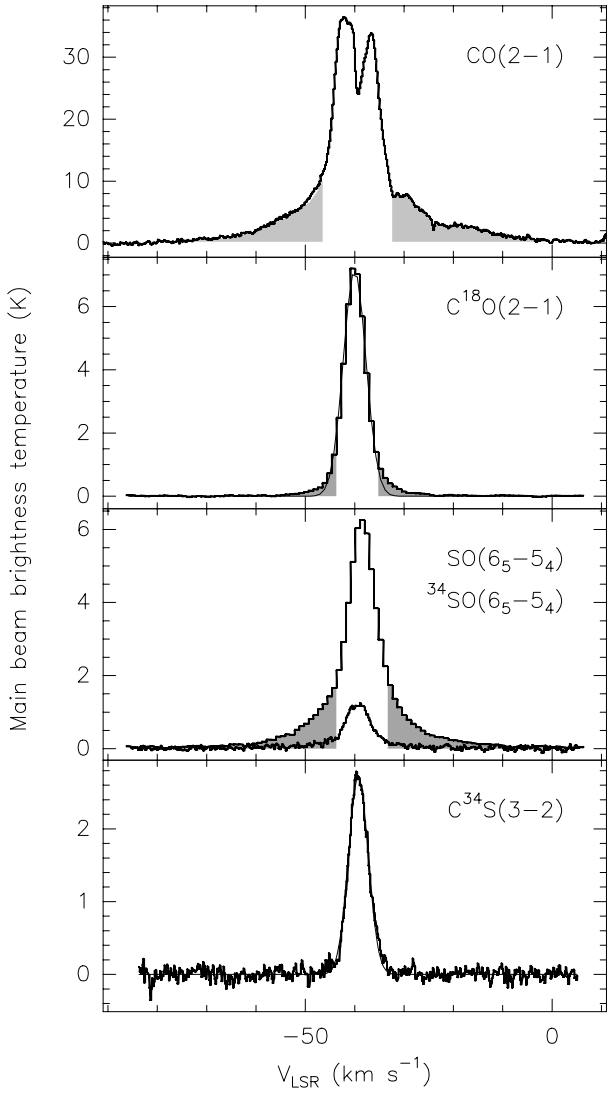


**Fig. 6.** CO(2–1), $C^{18}O$(2–1), SO($6_5$–$5_4$), $^{34}$SO($6_5$–$5_4$) and $C^{34}S$(3–2) spectra towards the peak of molecular emission in IRAS 12326–6245. The shaded areas show the blue- and red-shifted parts of the SO($6_5$–$5_4$) and $C^{18}O$(2–1) spectra (see text). For $C^{18}O$(2–1) and $C^{34}S$(3–2) single Gaussian fits are shown.

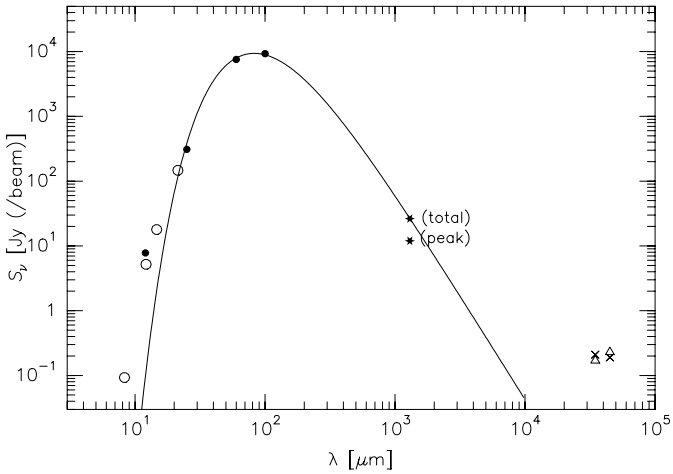


**Fig. 7.** Spectral energy distribution of IRAS 12326–6245 using our infrared data together with the information from the MSX catalog (○, Egan et al. 1999), the IRAS fluxes (●), our 1.3 mm continuum fluxes, and the free-free emission measured at radio wavelengths by Walsh et al. (1998). In addition, we show a modified black-body curve (solid line). The fit parameters are a temperature of 60±7 K and an index $\beta$ for the wavelength-dependent absorptivity of 1.2±0.5.

of $T_{\rm dust}$ = 50 K for the core since the hot environment of O and early B type stars fills only a small percentage of the beam (see also the black-body fit to the SED in Sect. 4.1). For the more extended gas component, we adopted an average temperature of $T_{\rm dust}$ = 30 K.

In addition, the source-averaged molecular hydrogen column density for the core was determined from the $\lambda$1.3mm continuum measurements (Henning et al. 2000a). We estimated a value of $N(H_2)_{(1.3{\rm mm})}$ = 6.25 $10^{23}$ cm$^{-2}$ for IRAS 12326–6245 which is one order of magnitude larger then the estimates found by Henning et al. (2000a) for comparable massive star-forming regions.

In order to estimate the volume-averaged hydrogen number density $n(H_2)$ from our 1.3 mm continuum measurements, we assume that the source has the same extent along the line of sight as in the plane of the sky. Based on the barely resolved Gaussian core profile in the NE–SW direction, a beam-deconvolved source size of 7.3″ was determined from the FWHM of the Gaussian core, if we use a beam size (HPBW) of 23″. Since, the Gaussian core profile in the NE–SW direction is unresolved, we assumed a mean beam-deconvolved source size of ≈ 6.5″. The result is $n(H_2)$ = 3.5 $10^7$ cm$^{-3}$ which implies a very high central core density in a rather large volume (source size of 6.5″ is equal to 0.49 pc in a distance of 4.4 kpc) compared to other well-known high-mass star-forming regions, like e.g. Orion IRc2 or W3 IRS5. If we use the beam-convolved source size of 23″, $n(H_2)$ amounts to a much lower value of $n(H_2)$ = 8 $10^5$ cm$^{-3}$. Based on the large distance and the low angular resolution of the 1.3 mm continuum measurements, a clear distinction of both the core component and the envelope is not possible. However, the strong intensity contrast between the extended emission and the central component implies that most of the core emission is dominated by radiation from dense and warm regions being the birth places of very young massive stars. In this respect, we note that all $N$- and $Q$-band objects (as well as both UC H II regions) shown in Fig. 4 are located in a region covered by the 23″ beam.

The $H_2$ column density and the mass can be also determined by the presumably optically thin $C^{18}O$ emission. Simple LTE estimates give the relation

$$N_{\rm L}(C^{18}O) \approx 7.8\,10^{14} \int T_{\rm mb} dv \qquad [{\rm cm}^{-2}] \tag{1}$$

assuming an excitation temperature of $T_{\rm ex} = 50$ K, which is similar to the relation based on LVG calculations by Mauersberger et al. (1992). This value of $T_{\rm ex}$ is close to the CO peak brightness temperature. The $N_{\rm L}(C^{18}O)$ estimate changes by less than a factor of 2 when $T_{\rm ex}$ varies between 10 and 100 K. The

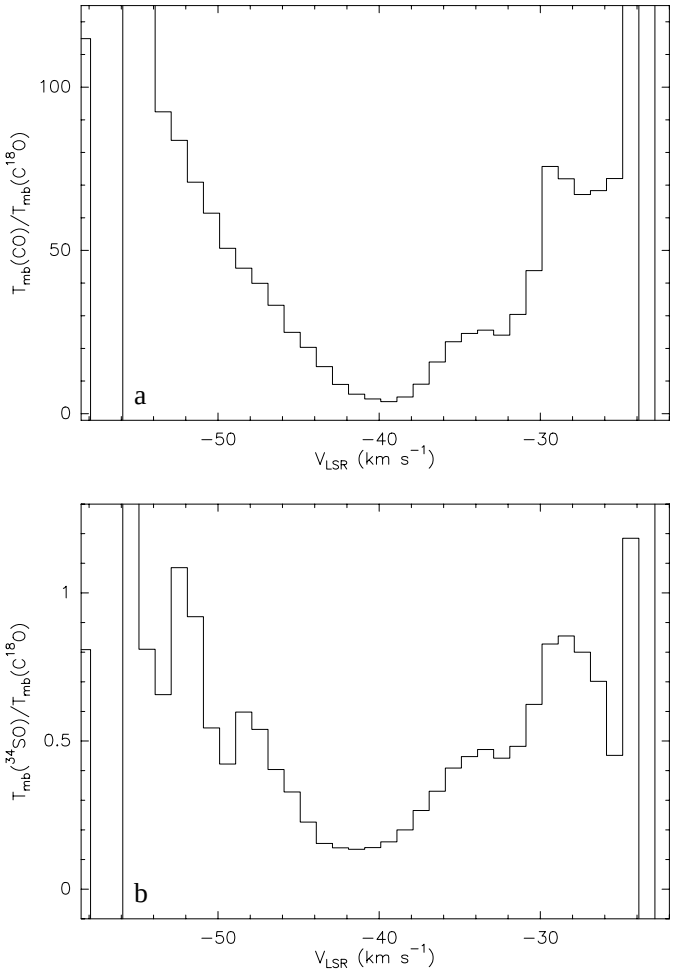


**Fig. 8a and b.** Ratio of the brightness temperatures in for CO(2–1):C$^{18}$O(2–1) **a** and for $^{34}$SO:C$^{18}$O(2–1) **b** as a function of the LSR velocity.

hydrogen column densities and masses are derived under the assumption of a C$^{18}$O relative abundance of $\chi(\mathrm{C^{18}O}) = 1.7\,10^{-7}$ (Frerking et al. 1982). For the hydrogen column density, we obtain $N(\mathrm{H_2})$ = 2.0 $10^{23}$ cm$^{-2}$. This value is quite similar to the estimate we obtained from the dust continuum measurement. The beam-averaged extinction can be estimated from the relation by Frerking et al. (1982) and ranges between 200 (from C$^{18}$O) and 600 mag (from continuum measurements).

The masses were determined from

$$M = \mu m d^2 \sum_i N_L^i(\mathrm{H_2})\Delta\Omega_i, \qquad (2)$$

where $m$ is the mass of the hydrogen molecule, $\mu$ is the ratio of total gas mass to hydrogen mass, $\mu \approx 1.36$ (e.g. Hildebrand 1983), and $\Delta\Omega_i$ is the pixel size ($10'' \times 10''$ in our case). In this way we obtain $M \approx 2600$ M$_\odot$ within the C$^{18}$O(2–1) map which is covering only the central cloud core. This is remarkably close to the core mass derived from the dust emission. However, taking into account the difference in the peak gas column densities derived from C$^{18}$O(2–1) and the dust emission this coincidence can be explained only by different source sizes in C$^{18}$O(2–1) and in the 1.3 mm continuum. In fact the "average" C$^{18}$O(2–1) FWHM is 34″ which is much larger than that of the continuum emission. Using the virial theorem (density gradient of $p$ = 2, line width of $\Delta$V = 8.7 km s$^{-1}$, and radius of $r$ = 50″ of an spherically symmetric cloud model), we obtain a virial mass for the whole cloud of $10^4$ M$_\odot$ which agrees very well with the total mass derived from the $\lambda$ 1.3 mm continuum which includes core and envelope.

### *4.3. Outflow*

The data clearly show the presence of a high-velocity molecular outflow. The terminal line of sight velocity reaches $\sim 40$ km s$^{-1}$ relative to the bulk of the cloud (from the CO(2–1) and SO data). The CO(2–1), SO, and C$^{18}$O(2–1) "wing" maps show that the direction of this outflow is approximately SE–NW and roughly perpendicular to the major axis of the dense core traced in CS, in the $\lambda$ = 1.3 mm continuum emission, and in the bulk of the C$^{18}$O(1–0) emission mapped by Lapinov et al. (1998).

The Figs. 4a and 5 clearly show that the centre of the outflow probably coincides with the southern UC H II region which is also the strongest infrared source in the $N$ and $Q$ bands. However, it is necessary to note that the positional uncertainties of the SEST maps can be substantial on this scale.

The outflow is most pronounced in the CO and SO lines (as well as in the SiO lines measured by Harju et al. 1998). However, the CO(2–1) and SO lines can be hardly used for a derivation of outflow mass and related parameters due to the apparently high optical depths and the uncertain SO abundance in shocked gas. This fact is illustrated by Fig. 8 where we plot ratios of the main beam brightness temperatures in CO(2–1) and C$^{18}$O(2–1) as well as in $^{34}$SO and C$^{18}$O(2–1), respectively, as a function of the velocity.

Fig. 8a shows that the CO(2–1)/C$^{18}$O(2–1) brightness ratio increases with increasing flow velocity and reaches a value of $\sim 100$ in the outer wings. This means that the optical depth in CO(2–1) decreases with increasing velocity but still remains very high even in the wings because the ratio is still much lower than the abundance ratio (the terrestrial value is $\sim 490$). A simple estimate shows that $\tau(\mathrm{CO}) \sim 5-10$ in the wings (assuming similar excitation for both isotops).

Both the C$^{18}$O(2–1) and $^{34}$SO lines are presumably optically thin so that strong variations of their intensity ratio most probably reflect variations in abundance ratio because changes in excitation lead only to moderate changes in intensities. Therefore, Fig. 8b shows that the SO/CO abundance ratio increases significantly with the flow velocity (by about an order of magnitude in the wings). This is in qualitative agreement with observations of other outflows (e.g. Chernin et al. 1994).

Apparently better estimates of the outflow parameters can be obtained from C$^{18}$O where the abundance is rather constant and the emission is optically thin. For this purpose, we constructed an integrated (over the source) C$^{18}$O(2–1) spectrum plotted in Fig. 9. The quantity plotted here is $\sum_i T_{\mathrm{mb}}^i \Delta\Omega_i$. It is proportional to the mass per unit velocity interval.

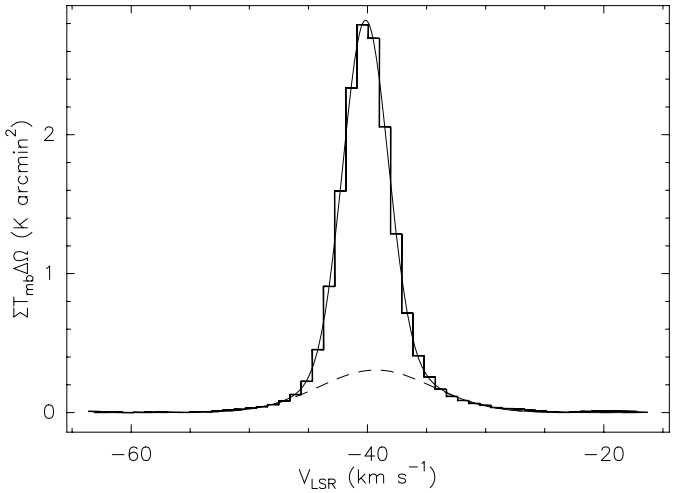


**Fig. 9.** The integrated $C^{18}O$(2–1) spectrum multiplied by the pixel size. The thin solid line represents a 2-dimensional Gaussian fit. The dashed line shows the broad Gaussian profile separately.

This spectrum can be well fitted by two Gaussians with different widths as shown in Fig. 9. It seems to be reasonable to identify the broad component ($\Delta V \sim 11$ km s$^{-1}$) with the outflow. Another approach is that the emission from outflowing gas is identified with residual "wings" in the line profile after subtraction of a single Gaussian. In this case the velocity distribution of the outflowing gas is arbitrarily "zeroed" at lower velocities which cannot be justified by the data. Therefore this approach gives essentially a lower limit for the outflow mass. In the following we shall call it the "traditional" estimate. A detailed discussion of the amount of high-velocity emission within the ambient cloud line core and the uncertainties of different approaches to derive flow parameters can be found in the paper by Cabrit & Bertout (1990).

In the following, we give two sets of the estimates for physical parameters: (1) the "traditional" one which refers to the gas producing wings in the line profile above a single Gaussian and (2) that which refers to the broad Gaussian component in the Gaussian fit. We shall call it the "Gaussian" estimate. In the latter case we subtract from the source-integrated spectrum the narrow ($\Delta V$ = 4.5 km s$^{-1}$) Gaussian component.

The main integral outflow parameters are mass ($M_{\rm f}$), mechanical momentum ($P_{\rm f}$), and kinetic energy ($E_{\rm kin}$). From the residual $C^{18}O$ spectrum, we can derive these quantities per unit velocity interval under the same assumptions as above. In this way, we obtain $dM/dV$ from Eq. (2) applying it to an unit velocity interval, $dP/dV = (V - V_0)dM/dV$ and $dE_{\rm kin}/dV = 0.5(V - V_0)^2 dM/dV$. These quantities are plotted in Fig. 10. The shaded areas are used to derive the integral parameters in the "Gaussian" (G) approach. The heavily shaded areas correspond to the "traditional" (T) approach. From the 2-component Gaussian fit, we obtain: $M_{\rm f}^{\rm (G)} \approx 600$ M$_\odot$, $|P_{\rm f}^{\rm (G)}| \approx 4400$ M$_\odot$ km s$^{-1}$, and $E_{\rm kin}^{\rm (G)} \approx 25000$ M$_\odot$ km$^2$ s$^{-2}$ $\approx 1.5\,10^{47}$ erg. The outflow is neither located in the plane of the sky nor completely perpendicular to that plane. Here we assumed a value of 57.3° relative to the plane which is the average value for a uniform distribution of random orientations.

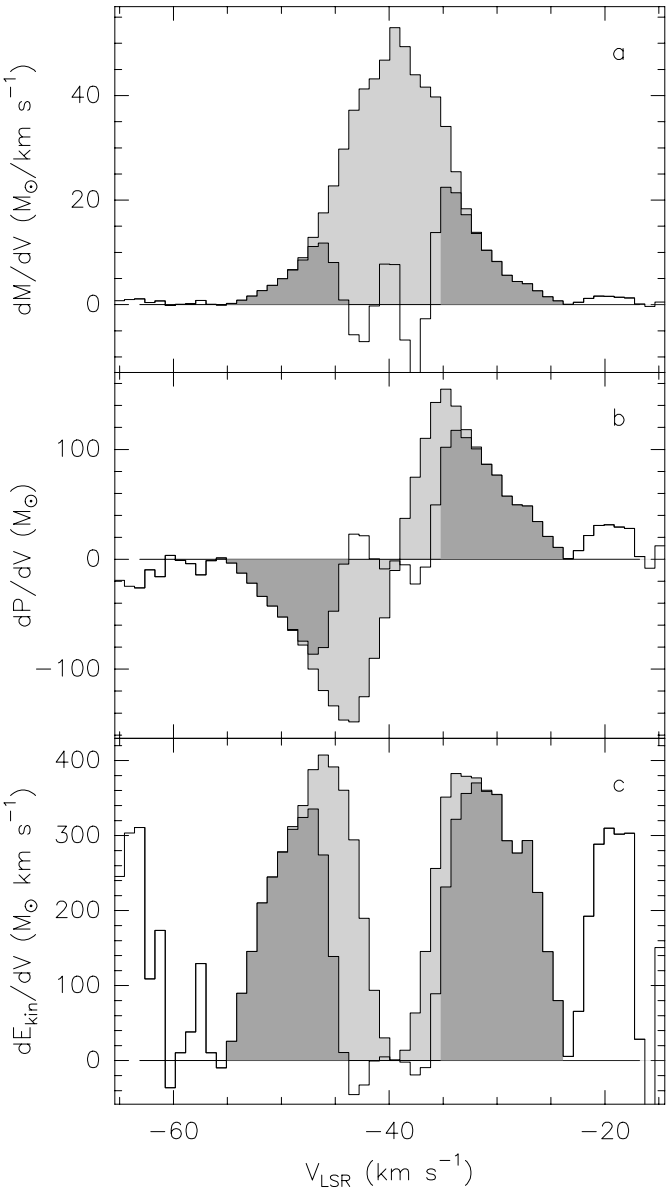


**Fig. 10a–c.** The outflow mass in **a**, the mechanical momentum in **b**, and the kinetic energy in **c** per unit velocity interval are shown as function of the LSR velocity. The light-shaded areas are used to derive the integral parameters in the "Gaussian" (G) approach. The dark-shaded areas correspond to the "traditional" (T) approach (see Sect. 4.3).

The mass estimate for the "traditional" approach is much lower, $M_{\rm f}^{\rm (t)} \approx 160$ M$_\odot$. For the momentum we get $|P_{\rm f}^{\rm (t)}| \approx 2200$ M$_\odot$ km s$^{-1}$ and for the kinetic energy $E_{\rm kin}^{\rm (t)} \approx 18200$ M$_\odot$ km$^2$ s$^{-2}$. The mass of the outflow can also be estimated from the CO(2–1) map (Fig. 4a) (see, e.g., Henning et al. 2000a). Here, we obtain a value of 320 M$_\odot$, well in the range of the above estimates. The momentum $|P_{\rm f}^{\rm (t)}|$ we get from the CO(2–1) map is 5000 M$_\odot$ km s$^{-1}$ comparable with the "Gaussian" estimate.

Other often determined outflow parameters are the dynamical timescale $t_{\rm d}$, the mass outflow rate $\dot{M} = M_{\rm f}/t_{\rm d}$, the force or momentum supply rate $F = P_{\rm f}/t_{\rm d}$, and the mechanical luminosity $L = E_{\rm kin}/t_{\rm d}$. The dynamical flow age is not a very well-defined quantity. It would be better to replace this quantity by the *time* in which the "information" travels from the central source to the most distant points of the outflow. However, such an estimate is not yet possible because the information speed cannot be directly estimated from the observational data.

For the sake of comparison with estimates in the literature, we derived the dynamical timescale by the expression $t_{\rm d} = R_{\rm f}/\langle V \rangle$, where $R_{\rm f}$ is assumed to be equal to half of the distance between the high-velocity emission peaks and $\langle V \rangle = P_{\rm f}/M_{\rm f}$ (e.g. Cabrit & Bertout 1990; Shepherd & Churchwell 1996a,b). The separation between the peaks of the blue-shifted and red-shifted emission is $\sim 10''$ in $C^{18}O$ but much lower in SO. An estimate of the average velocity $\langle V \rangle$ is very different for the two approaches outlined above due to the difference in mass estimates. With the "traditional" approach we obtain $R_{\rm f} \sim 0.1$ pc, $\langle V \rangle \sim 8$ km s$^{-1}$ and $t_{\rm d} \sim 10^4$ years without correction for the inclination angle. With an inclination angle of 57.3°, we obtain 7 $10^3$ years. Then, the other parameters are the following: $\dot{M} \sim 0.02$ M$_\odot$/yr, $F \sim 0.15$ M$_\odot$km s$^{-1}$/yr and $L \sim 100$ L$_\odot$. All these values are among the highest known from the literature for objects of similar luminosity (see Shepherd & Churchwell 1996a,b; Acord et al. 1997; Henning et al. 2000a). The origin of the outflow must be very close to the mid-infrared sources. The near-infrared nebulosity points to the northern UC H II region as the origin of the outflow. However, without interferometric measurements of the outflow, the question from which source the outflow exactly comes cannot be finally answered.

## 5. Conclusions

We presented a multi-wavelength study of the region around the luminous IRAS source 12326–6245. Mid-infrared imaging revealed the presence of a deeply embedded proto-Trapezium system surrounded by a cluster of near-infrared sources. Two of the members of the Trapezium system are associated with UC H II regions detected by Walsh et al. (1998). The exciting stars of the two UC H II regions are of very similar spectral type (B0) if we assume that only one star dominates the energetics of each region and dust extinction in the ionized gas is of minor importance.

The molecular line maps led to the detection of one of the strongest molecular outflows in the southern sky. We obtain a mass loss rate of about $\dot{M} \sim 0.02$ M$_\odot$/yr, a momentum rate of $F \sim 0.15$ M$_\odot$km s$^{-1}$/yr and a mechanical luminosity of $L \sim 100$ L$_\odot$.

*Acknowledgements.* We are grateful to the SEST staff for help with the observations. The work was supported in part by the INTAS grant 93-2168-ext and grants 96-02-16472, 99-02-16556 from the Russian Foundation for Basic Research and by DFG grant He 1935/14-1. This research has made use of the Simbad database, operated at CDS, Strasbourg, France. We acknowledge the observing time for IRAC2b and MANIAC imaging granted by the MPI for Astronomy (Heidelberg).

## References

Abt H.A., 1986, ApJ 304, 688
Acord J.M., Walmsley C.M., Churchwell E., 1997, ApJ 475, 693
Böker T., Storey J.W.V., Krabbe A., Lehmann T., 1997, PASP 109, 827
Booth R.S., Delgado G., Hagström M., et al., 1989, A&A 216, 315
Bonnell I.A., Bate M.R., Zinnecker H., 1998, MNRAS 298, 93
Braz M.A., Epchtein N., 1983, A&AS 54, 167
Braz M.A., Epchtein N., 1987, A&A 176, 245
Cabrit S., Bertout C., 1990, ApJ 348, 530
Caswell J.L., 1998, MNRAS 297, 215
Caswell J.L., Haynes R.F., 1987, Aust. J. Phys. 40, 215
Caswell J.L., Vaile R.A., Ellingsen S.P., Whiteoak J.B., Norris R.P., 1995, MNRAS 272, 96
Chernin L.M., Masson C.R., Fuller G.A., 1994, ApJ 436, 741
Chini R., Krügel E., Kreysa E., 1986, A&A 167, 315
Cohen R.J., Baart E.E., Jonas J.L., 1988, MNRAS 231, 205
Egan M.P., Price S.D., Moshir M.M., et al., 1999, Air Force Laboratory Technical Report No. AFRL-VS-TR-1999-1522
Emerson D.T., Klein U., Haslam C.G.T., 1979, A&A 72, 234
Frerking M.A., Langer W.D., Wilson R.W., 1982, ApJ 262, 590
Garay G., Lizano S., 1999, PASP 111, 1049
Griffin M.J., Orton G.S., 1993, ICARUS 105, 537
Gürtler J., Henning Th., Krügel E., Chini R., 1991, A&A 252, 801
Harju J., Lehtinen K., Booth R., Zinchenko I., 1998, A&AS 132, 211
Henning Th., Pfau W., Altenhoff W.J., 1990, A&A 227, 542
Henning Th., Schreyer K., Launhardt L., Burkert A., 2000a, A&A 353, 211
Henning Th., Klein R., Launhardt R., Schreyer K., Stecklum B., 2000b, In: Lemke D., Stickel M., Wilke K. (eds.) ISO Surveys of a Dusty Universe. Springer-Verlag, Berlin, p. 333
Hildebrand H., 1983, QJRAS 24, 267
Jackson J.M., Armstrong J.T., Barrett A.H., 1984, ApJ 280, 608
Jijina J., Adams F.C., 1996, ApJ 462, 874
Kreysa E., 1990, In: ESA Proc. of the 29th Liege International Symposium. From Ground-Based to Space-Borne Sub-mm Astronomy. ESA SP-314, p. 265
Lapinov A.V., Schilke P., Juvela M., Zinchenko I., 1998, A&A 336, 1007
MacLeod G.C., Scalise E. Jr., Saedt S., Galt J.A., Gaylard M.J., 1998, AJ 116, 1897
Mauersberger R., Wilson T.L., Mezger P.G., Gaume R., Johnston K.J., 1992, A&A 256, 640
Moorwood A., Finger G., Biereichel P., Delabre B., 1992, The Messenger 69, 61
Ossenkopf V., Henning Th., 1994, A&A 291, 943
Osterloh M., Henning Th., Launhardt R., 1997, ApJS 110, 71
Pantin E., Starck J.-L., 1996, A&AS 118, 575
Shepherd D.S., Churchwell E., 1996a, ApJ 457, 267
Shepherd D.S., Churchwell E., 1996b, ApJ 472, 225
Shepherd D.S., Watson A.M., Sargent A.I., Churchwell E., 1998, ApJ 507, 861
Vacca W.D., Garmany C.D., Shull J.M., 1996, ApJ 460, 914
Walsh A.J., Burton M.G., Hyland A.R., Robinson G., 1998, MNRAS 301, 640
Watson A.M., Coil A.L., Shepherd D.S., Hofner P., Churchwell E., 1997, ApJ 487, 818
Wood D.O.S, Churchwell E., 1989, ApJS 69, 831
Zinchenko I., Mattila K., Toriseva M., 1995, A&AS 111, 95